Section 1
PROGRESS IN LASER FUSION

1.A Cryogenic Laser-Fusion Target Experiments

Direct-drive laser fusion is accomplished by uniformly illuminating spherical fuel-bearing pellets with high-power laser beams, causing their implosion and subsequent manyfold increase in density and temperature. Recently, short-wavelength lasers have been found to be capable of efficient compression of fusion pellets due to the creation of large ablation pressures (≥ 20 Mbar) while producing few suprathermal electrons, which tend to preheat the fuel and degrade the compression.[1,2] Eventually, for inertial confinement fusion (ICF) to become an economical method for producing power, a gain in energy in excess of 100 must be produced from a fusion pellet. It has been estimated that the DT fuel in such a pellet must be compressed to ~ 1000 times liquid density (XLD) and reach a temperature of 4 to 5 keV in the central region for thermonuclear ignition and efficient burn to occur.[3]

In order to obtain efficient compression of a target, the fuel should initially be at a low temperature and be compressed adiabatically. If enough fuel is compressed in this way and heating of the fuel occurs at the final stages of the implosion, then ignition of the fuel and a net gain of energy will occur. A simple way to achieve high compression of fusion fuel is to cool the target cryogenically so that the fuel is initially a solid levitated against the inside edge of the pusher. In addition to the low initial temperature, the solid state of the fuel makes it impossible for shocks propagating through the fuel layer to reach the origin and rebound, causing fuel preheat. Other requirements needed

to compress fusion fuel on a low adiabat are pulse shaping and low preheating of the fuel.[4]

In this article we describe direct-drive laser-fusion experiments performed on cryogenically cooled targets that were compressed by the short-wavelength (351-nm) beams of the OMEGA laser system. While not all of the necessary requirements for low-adiabat, nearly isentropic compression[4] are met in these experiments, the use of cryogenic targets makes it possible to study the performance of fusion-fuel targets designed to obtain high peak fuel densities. The targets consisted of simple glass microballoons filled with high-pressure DT gas. These targets were held in place on ultra-low-mass supports inside a cryogenically cooled housing positioned inside the OMEGA target chamber. The targets used in these experiments were prepared for an implosion experiment by a technique that optimizes the uniformity of the frozen-fuel layer.

Target performance was extensively characterized by a set of x-ray, plasma, and nuclear instruments. The x-ray and plasma diagnostics, which principally measured laser-target interaction, included the following: plasma calorimeters, charge collectors, an x-ray calorimeter, an x-ray microscope, a streaked x-ray spectrograph, and a time-resolved, soft x-ray diode array. Neutron and particle diagnostics, which were sensitive mainly to the thermonuclear reaction products, included the following: a set of neutron counters, a detector system for measuring the activation of target-shell material by the thermonuclear neutrons, knock-on detectors, and a set of neutron time-of-flight detectors. Typical target performance recorded was of $\sim 70\%$ absorption, maximum shell velocities of $\sim 3 \times 10^7$ cm s^{-1}, neutron yields of 10^6 to 10^8, and final fuel areal densities of 20 to 40 mg cm^{-2}. Fuel densities at the time of thermonuclear neutron production, estimated from measurements of fuel areal density (ρR), were in the range of 100 to 200 times the density of liquid DT for the optimum targets examined in these experiments.

Previous experiments[5] have reported fuel densities in the range of 100 XLD using nuclear activation techniques that measure the shell areal density ($\rho\Delta$R) of the material surrounding the compressed fuel. The compressed-fuel densities were inferred from the measured $\rho\Delta$R using the assumptions of mass conservation, a one-dimensional model of the compressed core, and pressure balance between shell and fuel. The measurements of ρR and inferred values of fuel density presented in this work are not dependent on assumed or actual values of shell areal density, temperature of the imploded material, or amount of fuel-shell mixing; they are the first such measurements of highly compressed thermonuclear fuel.

Experiments

1. Laser Conditions

Recent modifications of the OMEGA system that were used in these experiments include liquid-crystal polarizers,[6] which enabled circularly polarized radiation to be propagated through the entire front end of the amplifier system, thereby minimizing stress birefringence induced by

the rod amplifiers, and distributed phase plates, to increase the uniformity of the target irradiation.[7]

Typical performance of the OMEGA system during these experiments was with output energy of 125 J per beam at 1054 nm in a 750-ps pulse (FWHM), with a corresponding frequency-tripled output per beam of 75 J in a 650-ps pulse. Beam diameters were 17 cm (95% intensity) at the output of the frequency-tripling crystals. Individual beam energies were measured by reflection of a small fraction of the beam into integrating calorimeters that measured the 1ω, 2ω, and 3ω components of the conversion-crystal output with a beam-to-beam accuracy of 1% and an absolute accuracy of 1%–2%. The beam-on-target arrival time was adjusted to be coincident to within 3 ps. The per-beam energy on target was estimated by measuring the loss in energy incurred as the beam traveled from the output of the conversion crystals into the target chamber. As so estimated, the variation in beam-to-beam energy was reduced to an average of $\sim 5\%$ (σ_{rms}) for these experiments. The 24 beams of OMEGA were focused onto the target by *f*/3.7, 566-mm-focal-length, AR-coated-fused-silica, aspherical single-element lenses. Individual beam pointing was verified to an accuracy of ~ 10 μm or less of lateral displacement from the target center and ~ 50 μm or less of transverse displacement from the target center.

The on-target illumination uniformity was enhanced for these experiments by incorporating a distributed phase plate (DPP)[7] into each beam at the position of the final focus lens. The DPP's modify the phase front of the OMEGA beams (phase-front errors have been found to be the dominant source of intensity nonuniformities at the target plane[8]) by shifting the phase of the beam by a randomly assigned amount of either 0 or π in approximately 10,000 hexagonally shaped subregions of the beam. Each phase plate therefore produces the equivalent of 10,000 beamlets; the combined effect of the phase plates used in the 24 OMEGA beams is to irradiate the target with $\sim 240{,}000$ beamlets. The DPP's provide an improved target irradiation uniformity with a slight reduction ($\sim 20\%$) in the average intensity. The variation in illumination uniformity due to DPP-modified OMEGA beams has been estimated to be $\sim 8\%$ (σ_{rms}) if thermal smoothing in the plasma by 1% of the beam diameter (~ 3 μm) is assumed to occur.[7] In actual experiments a larger variation in intensity uniformity occurs, due principally to the beam-to-beam energy output variation [which was $<9\%$ (σ_{rms}) for all experiments]. The combined variation in intensity uniformity is therefore estimated to have been $\lesssim 12\%$ (σ_{rms}) for these experiments.

2. Targets

Implosion experiments were performed on simple glass microballoons containing DT at pressures of 75 to 100 atm. The targets were nominally filled with an equimolar mixture of deuterium and tritium. The targets were mounted, using no glue, on a support structure that was compatible with the cryogenic target-positioning system (Fig. 35.1).[9] The targets were supported by spider silks drawn across a *U*-shaped copper mount whose width (3 mm) and thickness

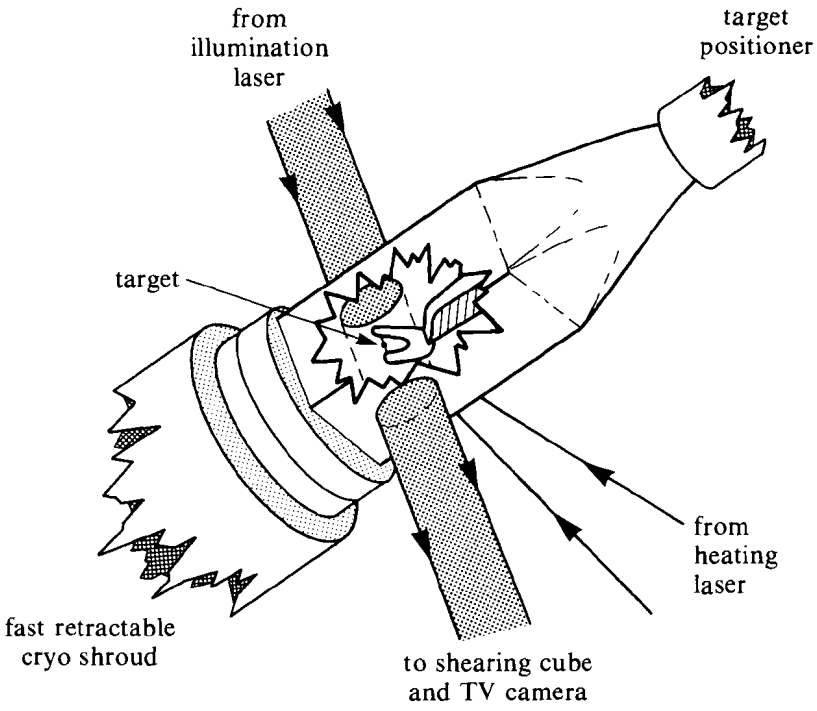

Fig. 35.1
Schematic of the target assembly as it would appear positioned inside the cooling shroud. The heating laser and interferometer system are used to optimize the thickness uniformity of the solid DT layer.

(100 μm) were constrained by the requirement that the horseshoe be narrow enough to fit in the liquid-He-cooled target shroud and thin enough not to obscure the converging OMEGA beams. A target was assembled onto its mount by placing it on a cradle consisting of two spider silks drawn across a *U* mount, after which additional spider silks (one to three) were placed over and under the target to hold it in place. Next, the target-mount assembly was coated with a 0.2-μm flash of parylene to give it additional mechanical stability.

3. Cryogenic Target System

Targets mounted as described above were positioned and cooled to below the freezing point of DT (19°K) by the OMEGA cryogenic target-positioning system (cryo system), which is described in detail in Ref. 11. The system consists of four subsystems: (1) a liquid He-cooled target positioner; (2) a fast, retractable, liquid-He-cooled shroud; (3) a heating laser system used to vaporize rapidly the frozen fuel while the target is inside the cooled shroud; and (4) a shearing interferometer system used to document the thickness and uniformity of the frozen fuel layer.

Preparation of the cryogenic target is based on the fast-refreeze technique developed by KMS Fusion.[10] Targets were prepared for implosion experiments as follows: The target was placed in the OMEGA chamber and cooled to below the DT freezing point in a

liquid-He-cooled shroud. The uniformity of the frozen-fuel layer was then optimized by repeatedly heating this layer with an Ar-ion laser, followed by rapid cooling, until a layer with good uniformity was obtained. [Figures 35.2(a) and 35.2(b) show interferograms of a cryo target before and after preparation by the fast-refreeze technique.] Estimates of the uniformity of the fuel layer obtainable with this technique were made by ray-tracing simulation. These simulations indicated that symmetry of the interferogram to within 0.5 fringes implied a fuel-layer uniformity with a $\leq 20\%$ variation in layer thickness. (This variation was the limit to which variations could be detected interactively and representative of the uniformity of the initial fuel layer in the implosion experiments.) Finally, ~ 40 ms before target irradiation, the cooling shroud was rapidly extracted, exposing the target to the ambient environment for ~ 10 ms. (The length of time required for the DT to melt was ~ 30 ms.)

Interferograms of 300-μm-diameter GMB with 5-μm DT layer

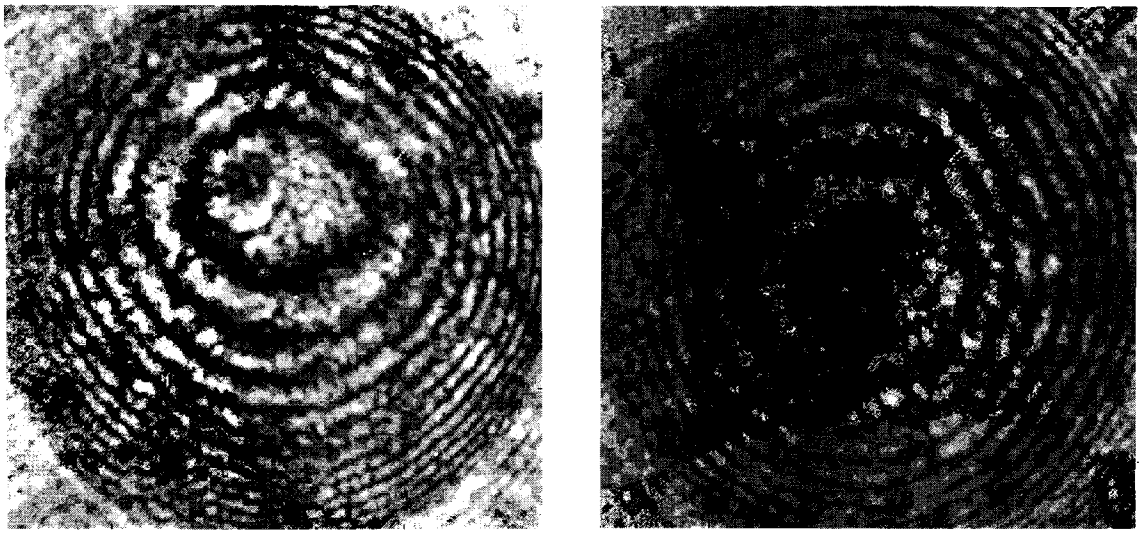

(a)
before refreeze

(b)
after refreeze

E4482

Fig. 35.2
Interferograms of a 300-μm-diameter glass microballoon (a) before and (b) after preparation by the fast-refreeze technique. The prepared target (b) has a nearly uniform solid DT layer with a thickness of 5 μm.

Target Design

Target design and prediction of target performance was accomplished with the one-dimensional (*LILAC*) and two-dimensional (*ORCHID*) hydrodynamic simulation codes. Both codes use tabular equation of state (SESAME),[11] flux-limited electron thermal transport, multifrequency group radiation transport with local thermodynamic equilibrium (LTE) opacities,[12] and inverse-bremsstrahlung-absorption energy deposition through a ray-tracing algorithm in the underdense plasma.

Figures 35.3(a)-35.3(f) show the *LILAC*-calculated target behavior for a typical cryo experiment. In this example, the target is a 150-μm inner radius (R_0) glass microballoon having a 5-μm wall (ΔR_0) and containing 100 atm of DT frozen into a 5-μm layer of ice. The target is assumed to be irradiated with 1200 J of UV radiation in a 650-ps (FWHM) Gaussian pulse, which was the typical illumination condition for these experiments. Figures 35.3(a) and 35.3(b) show the fuel-shell interface trajectory and the time history of the in-flight aspect ratio ($R/\Delta R$), respectively. Initially, the shell is compressed, reaching an aspect ratio of ~ 70 at ~ 500 ps before the peak of the pulse, followed by a continuous decompression of the shell, due to radiative heating, as the implosion progresses. The fuel and shell begin to accelerate rapidly at ~ 400 ps before the peak of the pulse. The fuel density ρ rises to a peak value of ~ 300 g cm^{-3} and reaches an average temperature of 0.5 keV during the stagnation phase [Fig. 35.3(d)]. Peak fuel and shell areal densities [Figs. 35.3(c) and 35.3(e)], ρR and $\rho \Delta R$, are ~ 150 and ~ 50 mg cm^{-2}, respectively. A neutron yield of 1.1×10^{10} is obtained within a 40-ps time interval, coinciding with the time of fuel coalescence at the origin and peak compression [Fig. 35.3(f)]. The average fuel density during the time of neutron production, $<\rho>_n$, is 210 g cm^{-3}, which is lower than the peak density of 300 g cm^{-3}. The other neutron-averaged quantities are

$$<T_i>_n = 1.2 \text{ keV},$$
$$<\rho R>_n = 140 \text{ mg cm}^{-2},$$
$$\text{and } <\rho \Delta R>_n = 36.0 \text{ mg cm}^{-2}.$$

Results

Cryogenic target experiments were performed on a large number (~ 100) of DT-filled glass microballoons. Optimum conditions for target performance and measurements were determined iteratively by performing implosion experiments and improving target experiment and/or measurement techniques, followed by repeated implosion experiments. Some target experiments were unsuccessful because of unrepeatable circumstances, such as laser-system misfires or target mispositioning during cryo-shroud retraction. Successful, well-diagnosed target experiments were performed principally on glass microballoons filled with 100 atm of DT, having radii of 100 to 150 μm and shell thicknesses of 3 to 7 μm. We have tabulated results of target experiments in Table 35.I for which a complete set of measurements was obtained. The columns of Table 35.I are (1) the OMEGA shot number; (2) the microballoon shell inner radius R_0 (μm); (3) the shell thickness ΔR_0 (μm); (4) the incident energy E_{inc} (J); (5a) the measured and (5b) the predicted absorbed energy E_{abs} (J); (6) the beam balance σ_{rms}(%); (7a) the measured and (7b) the predicted thermonuclear neutron yield Y_N; (8a) the measured and (8b) the predicted neutron-averaged fuel areal density $<\rho R>_n$ (mg cm^{-2}); and (9a) the inferred and (9b) the predicted neutron-averaged fuel density $<\rho>_n$ (g cm^{-3}).

As can be seen by comparing columns 5a and 5b of Table 35.I, the measured and predicted fractions of incident energy absorbed by the

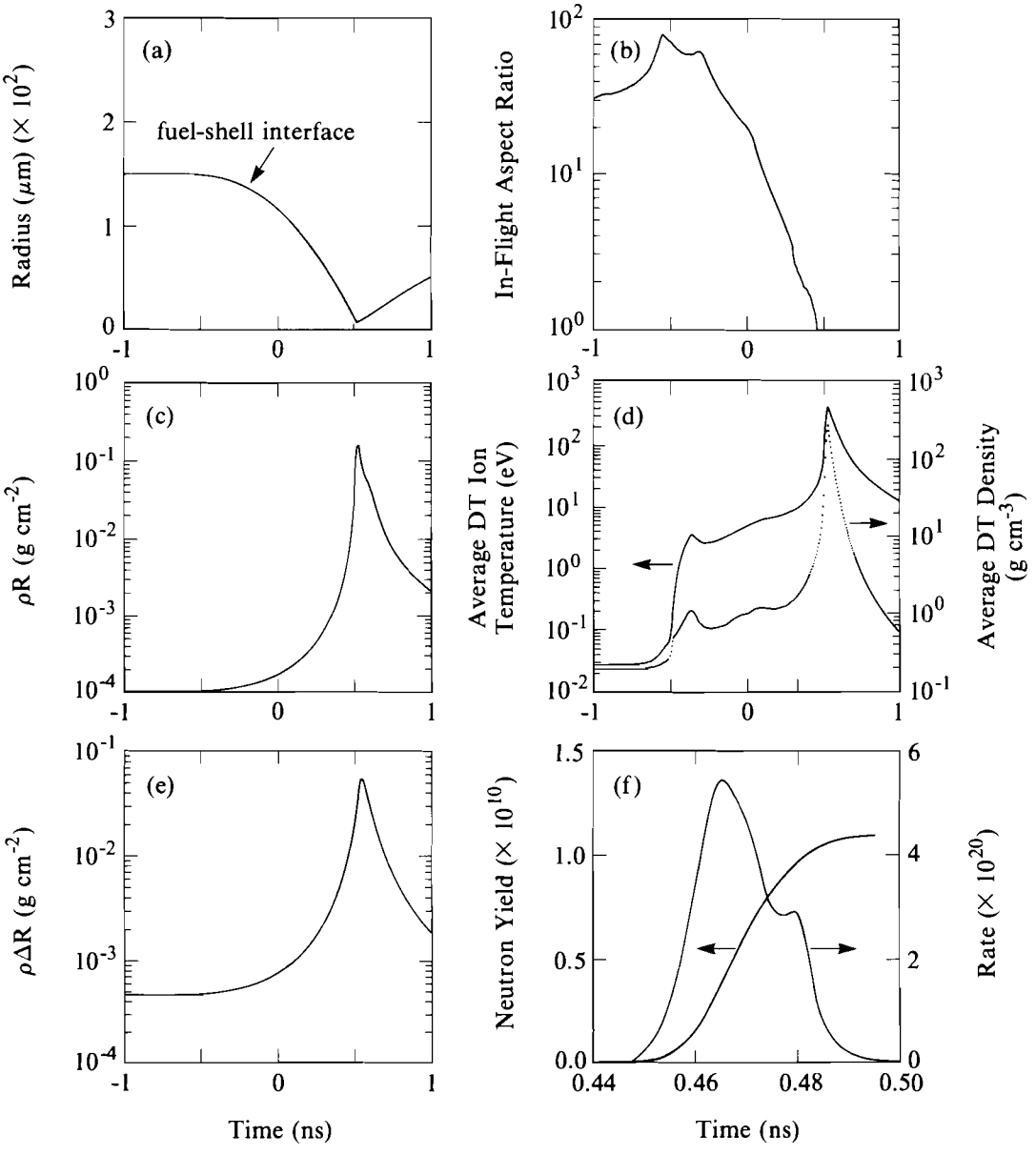

E4631

Fig. 35.3
One-dimensional hydrocode simulations (*LILAC*) of the implosion of a 300-μm-diameter, 5-μm-wall glass microballoon having a 100-atm-DT fill that has been cryogenically cooled, forming a 5-μm solid DT layer. (a) The fuel-shell interface trajectory. (b) The in-flight aspect ratio. (c) The fuel areal density. (d) The fuel temperature and density. (e) The shell areal density. (f) The integrated yield and rate of generation of neutrons during the time of peak compression.

Table 35.I
Cryogenic Experiment Results

(1) Shot	(2) R_o (μm)	(3) ΔR_o (μm)	(4) E_{inc} (J)	(5a) E_{abs} (J) expt	(5b) E_{abs} (J) *LILAC*	(6) σ_{rms} (%)	(7a) Y_N (n_o's) expt	(7b) Y_N (n_o's) *LILAC*	(8a) $<\rho R>_n$ (mg cm^{-2}) expt	(8b) $<\rho R>_n$ (mg cm^{-2}) *LILAC*	(9a) $<\rho>_n$ (g cm^{-3}) expt	(9b) $<\rho>_n$ (g cm^{-3}) *LILAC*
16011	192	2.8	–	1186	1176	4.1	8.3 (7)	5.9 (10)	4.4	43.4	0.8	23.8
16054	120	4.9	1080	747	780	4.9	9.2 (6)	1.4 (10)	32.0	96.2	30.0	158.0
16105	110	6.1	1066	768	828	8.7	4.7 (6)	6.2 (9)	35.5	68.1	40.4	107.0
16188	133	3.9	1065	793	764	5.2	1.4 (7)	2.9 (10)	16.6	135.0	11.3	261.0
16212	134	5.0	1138	858	875	7.4	6.4 (6)	1.2 (10)	27.8	130.0	20.9	216.0
16265	111	5.8	951	751	698	8.5	4.7 (6)	6.5 (9)	23.1	64.6	21.1	98.7
16266	137	5.7	1145	926	935	6.9	8.4 (6)	1.7 (10)	26.2	97.0	18.5	132.0
16267	134	5.8	1150	862	927	5.1	8.5 (6)	1.6 (10)	32.5	90.0	26.4	122.0
16268	134	5.7	1207	891	955	3.7	7.6 (6)	1.9 (10)	23.2	94.4	16.0	131.0
16270	103	5.2	1015	658	622	3.8	5.3 (6)	6.1 (9)	20.8	69.4	20.2	123.0
16272	118	7.0	1146	794	878	3.7	4.6 (6)	5.4 (9)	9.6	66.1	5.1	92.5
16279	128	5.9	1137	941	896	3.9	1.1 (7)	1.4 (10)	13.8	81.7	7.8	113.0

E4654

target are in close agreement. Independent measurements of the absorption, the x-ray conversion efficiency, and the mass-ablation rate versus intensity by glass targets irradiated by UV (351-nm) radiation[13] indicate that the partition of laser energy into these forms is well modeled by the one-dimensional code.

1. Time- and Space-Resolved X-Ray Measurements

The x-ray diagnostics are primarily sensitive to emission from the laser-heated shell material. Several of these diagnostics yield information about the state of the shell material during the course of the implosion. Figure 35.4 shows a set of images taken by an x-ray framing camera.[14] The framing camera consisted of a pinhole camera assembly with a 10-μm pinhole array illuminating a gated microchannel plate (MCP). Four x-ray images (frames) were obtained by independently gating four regions of the MCP with short ($\sim$200-ps) high-voltage pulses. The sensitive time of each frame was $\sim$120 ps (FWHM), and the frames were separated by 250 ps. There is some spatial smearing in these framed images because the target was in motion; nevertheless, a ring of emission is seen, the radius corresponding to the average shell radius during the frame. Figure 35.5 shows the measured and predicted radius of peak x-ray emission, as determined from framed x-ray images for three cryo target experiments where the target wall thicknesses were 3 μm, 5 μm, and 6 μm.

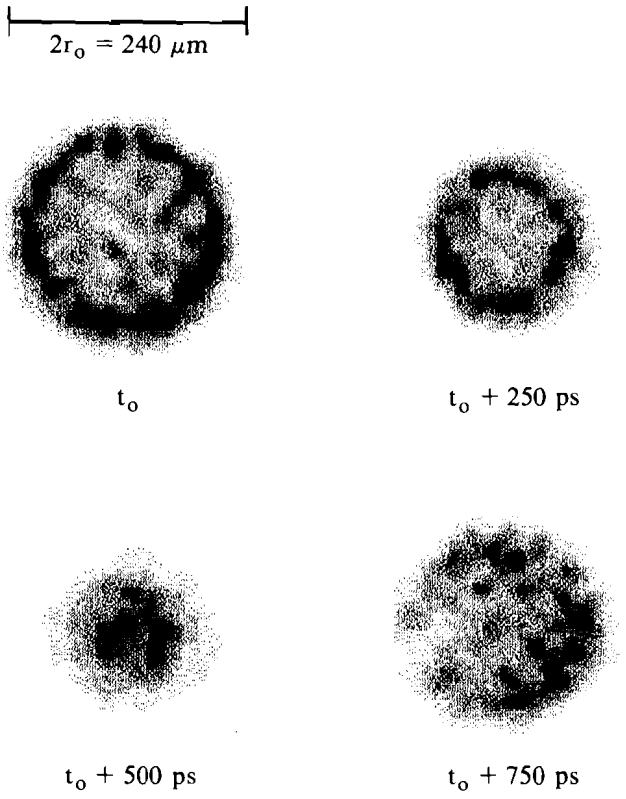

Fig. 35.4
X-ray images of a cryogenic target implosion taken with a four-frame x-ray-framing camera. The darker-shaded regions are the regions of highest x-ray emission. Small-scale structure is due principally to noise from the gated microchannel plate (MCP).

Further information about the implosion time history is obtained from measurements taken with the MINIFLEX soft x-ray photodiode system.[15] The MINIFLEX system consists of an array of four x-ray-sensitive photodiodes whose signals are read out by 3-GHz oscilloscopes, yielding spatially integrated, time-resolved (~200-ps FWHM) measurements of the x-ray emission. Figure 35.6 shows the time-resolved x-ray emission observed with MINIFLEX for the three target experiments of Fig. 35.5, together with *LILAC* predictions of the same. The measured and predicted curves were compared by normalizing the heights of the broad peak in the emission curve (corresponding roughly to the peak of the laser pulse) and by assuming these peaks to coincide in time. We see with these assumptions that the times of the measured and predicted stagnation peaks (Fig. 35.6) are nearly coincident. However, the height of the measured stagnation peak appears to deviate more for the thicker-shelled targets.

The size of the imploding shell as a function of time, as measured by the x-ray framing camera, and the time of shell stagnation, as measured by the MINIFLEX system, are in general agreement with the one-dimensional code predictions. The implosions are further diagnosed by analysis of high-resolution, hard x-ray images obtained

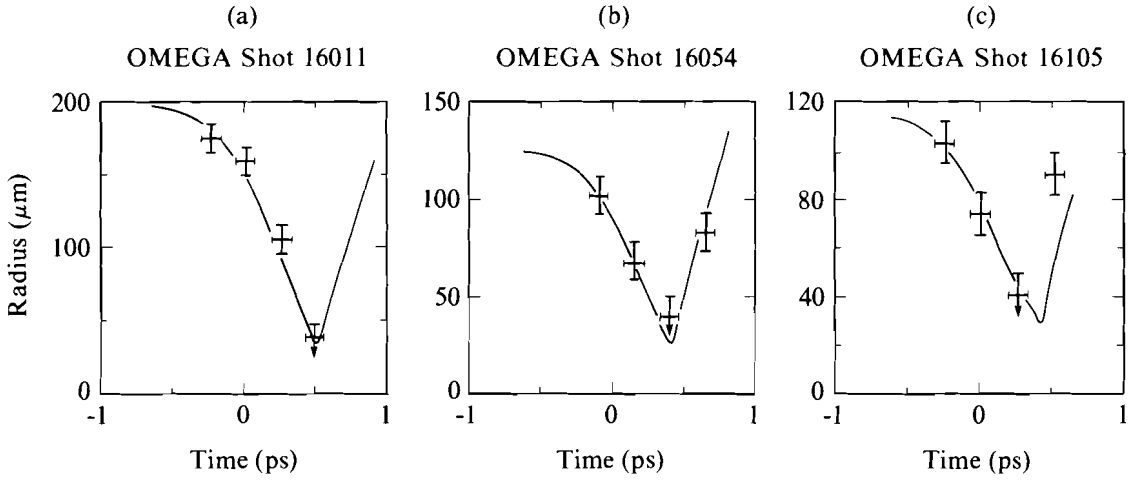

Fig. 35.5
Radius of peak x-ray emission versus time of three cryo targets having (a) 3-μm, (b) 5-μm, and (c) 6-μm walls, determined from framed x-ray images and as predicted by *LILAC*.

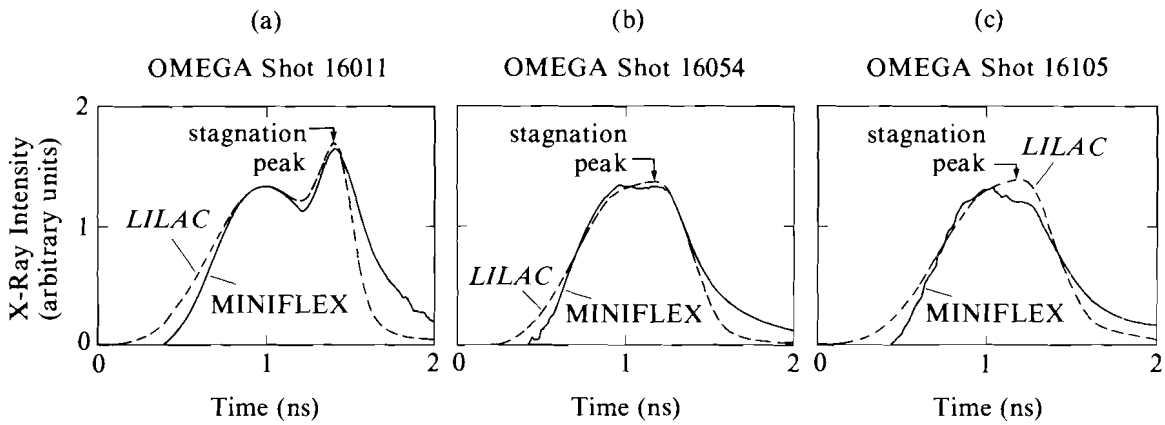

Fig. 35.6
Time-resolved spatially integrated x-ray fluence from cryo targets that have wall thicknesses of (a) 3 μm, (b) 5 μm, and (c) 6 μm, and *LILAC* prediction of same.

with a Kirkpatrick-Baez (KB) microscope,[16] which has a resolution of ~5 μm and records images on x-ray-sensitive film. The effective-energy range sampled in these images is 3.0 to 4.6 keV, limited at the low-energy end by transmission of the x rays through a metallic filter and at the high-energy end by reflection off the KB mirrors. Figure

35.7 shows the average radial profiles determined from KB microscope images of the same target experiments analyzed in Figs. 35.5 and 35.6, and from predictions of the same. The high-density regions at the center of the images are due to the continuum-dominated flux generated by shell stagnation. The predicted profiles all contain an outer peak at a radius that corresponds to the radius of peak emission (roughly the shell radius at the time of the peak of the pulse). An inner peak is present on the predicted profiles of the two thinner-shelled targets [Figs. 35.7(a) and 35.7(b)] but not on the predicted profile of the thicker-shelled target [Fig. 35.7(c)]. This is because the optical depth of the material is predicted to be high enough to prevent it from being seen. The measured profiles show stagnation region features that are smaller in radius than predicted. The measured profile of the thick-shelled target shows a central peak where none is predicted.

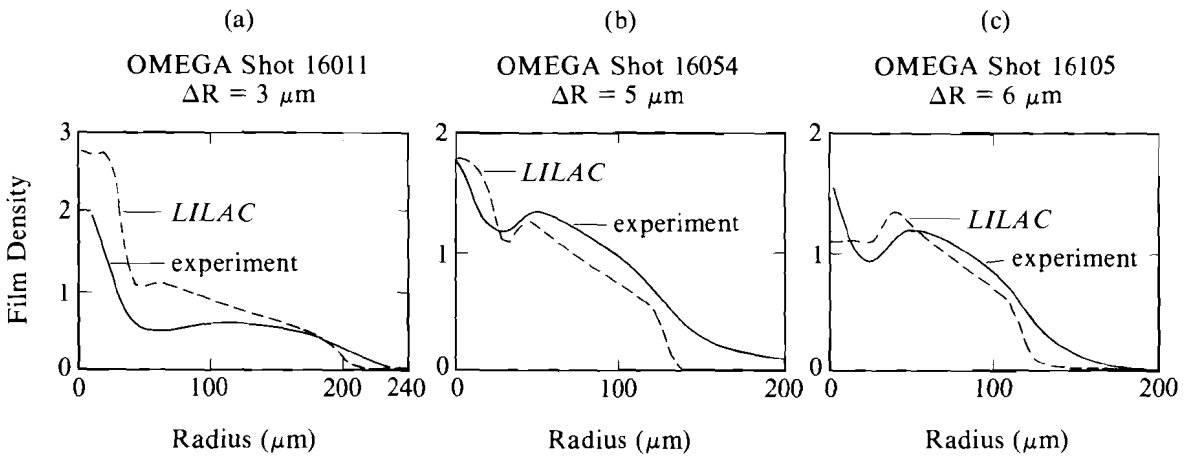

Fig. 35.7
Radial profiles determined from x-ray microscope images of cryo targets that have wall thicknesses of (a) 3 μm, (b) 5 μm, and (c) 6 μm, and *LILAC* prediction of same.

2. Neutron Yield

The total thermonuclear yield Y_N was measured for these experiments by a Cu activation system, an Ag activation system, and an array of neutron scintillator-photomultiplier pairs.[17] All of these yield-measuring systems were cross calibrated to the Cu activation system, which was absolutely calibrated. Errors in the measured yield for these experiments were primarily due to counting statistics. Figure 35.8 shows the normalized neutron yield (the measured neutron yield divided by the calculated yield) plotted as a function of the calculated convergence ratio C_R. (The convergence ratio is defined as the initial fuel-pusher interface radius divided by the minimum fuel-pusher interface ratio.) The normalized yields range from $\sim 3 \times 10^{-3}$ to $\sim 1 \times 10^{-4}$. The errors in the measured yield are, in general, much smaller than the scatter of the values. Previous measurements of the

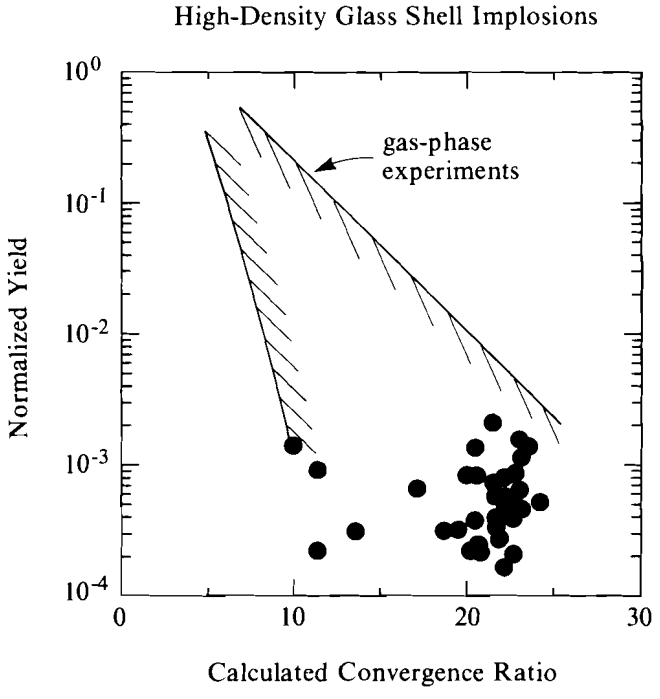

Fig. 35.8
Normalized neutron yield (ratio of experimentally measured yield to predicted yield) versus the calculated target convergence ratio (the ratio of the initial to final fuel-shell interface radius) for the cryogenic target experiments. The shaded region shows the range of normalized yields found for previous gas-phase experiments.

neutron yield produced by gas-phase targets illuminated by OMEGA[18-20] have shown that the normalized neutron yield is a decreasing function of C_R. In fact, the cryo experiments fall in the range of normalized yields observed for gas-phase target experiments (indicated by the shaded region in Fig. 35.8) where they overlap. The cryo targets, therefore, show normalized neutron yields that are similar to normalized yields observed from previous gas-phase target experiments, if targets having the same calculated convergence ratio are compared.

3. Fuel Areal Density

The fuel areal density ρR at the time of neutron yield (neutron-averaged ρR) was measured by the "knock-on" diagnostic technique.[21,22] This technique measures the number of deuterons and tritons in the compressed fuel that are scattered by 14.1-MeV fusion neutrons, the number of such ions (knock-ons) being directly proportional to the ρR. The ions were detected by stacks of polycarbonate (CR-39) track-detector foils, with metallic filters in front of and in between the foils. Three sets of knock-on detector foil-filter stacks were positioned at nearly mutually orthogonal positions around the target, both to increase the solid angle of the collector and to provide as representative a sample of the average knock-on flux as possible. Deuterons and tritons were distinguished from other particles (e.g., protons) by placing a criterion on the tracks left in the foils.

Only tracks with diameters exceeding a specified minimum diameter, which completely penetrated an individual foil, were counted as being left by knock-ons. These criteria limited the knock-ons detected in a single foil to a known, finite-energy window.[21]

The knock-on energy spectrum was sampled over a broad range by using metallic filters to slow down the knock-ons so that their energy was in the energy window defined by the track selection criteria. We used a stack of metallic filters and five CR-39 foils, which sampled the knock-on spectrum in five nearly independent energy intervals. We found that, although the position of the deuteron peak and hence the fraction of the total number of deuterons detected in any one foil differs depending on the amount of slowdown in the target, the sum of the knock-ons detected in four of the five foils is a nearly constant fraction, $f_D = 0.085$, to within $\pm 5\%$, for $\rho R_{\text{total}} \leq 50$ mg cm^{-2} ($\rho R_{\text{total}} = \rho R + \rho \Delta R$). This is an upper bound on f_D, which is independent of ρR_{total}, temperature of the fuel, or the amount of fuel-shell mixing. (Further details of this analysis will be explained in an upcoming LLE Review article.) The fuel areal density was obtained from the number of detected deuteron tracks by

$$\rho R = 5.4 \times 10^3 \frac{K_D}{Y_N} \left(\frac{4\pi}{\Delta \Omega} \right) \frac{1}{f_D} \quad ,$$

where K_D is the sum of the knock-on tracks detected in the four foils, $\Delta \Omega$ is the solid angle subtended by the foils, and Y_N is the neutron yield. Since f_D appears in the denominator of this expression and we use an upper bound of its value, we are able to obtain a lower bound on ρR.

Figure 35.9(a) shows the measured fuel areal densities plotted versus the calculated convergence ratios. (The error bars are calculated from the combined relative errors in measurement of the neutron yield and the knock-on flux.) The highest values of ρR are in the range 20 to 35 mg cm^{-2}, which were obtained by targets whose calculated convergence ratios are in excess of 20.

4. Fuel Density

The fuel density averaged over the time of thermonuclear burn (neutron-averaged ρ) can be estimated from the measured ρR by assuming a simple model for the distribution of the fuel. One such model (the "ice-block" model) assumes that the fuel has a constant density and is compressed into a region of radius R, and that neutrons are produced at the center of this region.[23] Assuming that all of the initial mass of the fuel, M, is compressed into this region, then the fuel density can be expressed as $\rho = (4\pi/3M)^{1/2} (\rho R)^{3/2}$. Although this is a simple model that is not expected to accurately describe the actual fuel distribution, it does give a conservative estimate of the fuel density. As an example, if the neutron production were constant across the fuel volume, the resulting inferred density would be $\sim 50\%$ higher than would be inferred by the ice-block model. The fuel densities inferred from the measured ρR, using the ice-block model, are shown in Fig. 35.9(b). The highest inferred fuel densities are in the range of 20 to 40 g cm^{-3} (100 to 200 XLD), again obtained with targets whose

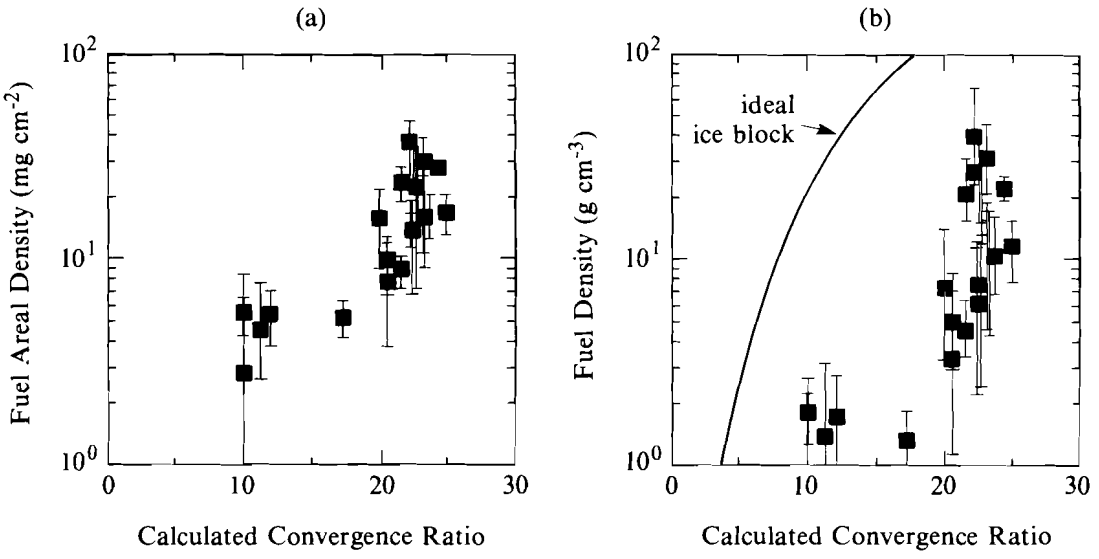

Fig. 35.9
(a) The measured fuel areal densities and (b) the inferred neutron-averaged fuel densities. The line in (b) indicates the maximum density that could be obtained for a given convergence ratio.

calculated convergence ratios are in excess of 20. The curve in Fig. 35.9(b) shows the density that would be obtained if all of the fuel were to be uniformly compressed to the calculated convergence ratio (assuming 100-atm initial fuel pressure).

Discussion

The amount of energy absorbed by the cryo targets was measured and found to be in good agreement with the predicted absorbed energy (Table 35.I). The time history of the cryo target implosions was diagnosed by measurements of the shell size versus time determined from x-ray framing camera images and by measuring the time of shell stagnation from x-ray photodiode measurements. These measurements indicate that the cryo targets are imploding nearly as predicted by the one-dimensional code *LILAC*. The measured neutron yields [Table 35.I, col. 7(a)] and the measured fuel areal densities [Table 35.I, col. 8(a)], however, fall below the predicted values. It has been pointed out previously[21] that the falloff of neutron yield with an increasing convergence ratio could be explained by illumination nonuniformities of the OMEGA system. As is seen in Fig. 35.8, the cryo target experiments show a similar trend, indicating that their performance was degraded by a similar mechanism. Deviations of both the measured size of the x-ray stagnation peak (Fig. 35.6) and the shape of the emission from the stagnating core (Fig. 35.7) from predictions indicate that although the shell and fuel are reaching maximum compression when predicted, the shell and fuel may still not be integral. The illumination nonuniformities known to remain in the

OMEGA system may be causing early implosion of some shell material, mixing of shell material, and a subsequent reduction in neutron yield. If neutrons are generated earlier than predicted (for instance, by early stagnating material), then the fuel will have reached a substantially lower areal density [see Fig. 35.3(c)], since the fuel areal density is predicted to increase by more than an order of magnitude within a very short time (~ 50 ps). The critical timing of the neutron burst with respect to the time of peak density attainment may be the dominant effect explaining the scatter of the measured fuel areal densities versus the convergence ratio [Fig. 35.9(b)]. Or, if pusher material has mixed into the fuel, it is expected that the actual convergence ratio achieved would be lower than predicted, again resulting in lower measured and inferred densities.

Summary

A series of direct-drive, ablatively driven implosion experiments were carried out on the 24-beam, 351-nm OMEGA laser system using cryogenic DT glass microballoons. Distributed phase plates were used to improve the target irradiation uniformity. Typical measured absorption fractions of 60% to 80% agreed with predicted values of this quantity. Time-resolved x-ray measurements showed that shell radius versus time and the time of shell stagnation were in good agreement with one-dimensional simulations. These results indicate that average features of the implosions are being accurately modeled by one-dimensional simulations.

Deviations from one-dimensional performance were seen in the shapes of the x-ray-emitting regions of the stagnating shell material, the height of the x-ray stagnation peak, the neutron yield, and the fuel areal density. It is likely, although not certain, that these effects result from nonuniform implosion of fuel and shell material due to residual nonuniformities in the OMEGA laser irradiation on target. Nevertheless, fuel areal densities of 20 to 35 mg cm^{-2} were measured using the knock-on diagnostic technique, implying neutron-averaged fuel densities of 20 to 40 g cm^{-3} (100 to 200 XLD). These experiments have resulted in the first direct measurements of the fuel areal density of highly compressed fusion fuel that do not involve any assumptions about temperature or fuel-shell mixing. The inferred fuel densities are the highest attained for any direct-drive laser-fusion experiments.

ACKNOWLEDGMENT

This work was supported by the U.S. Department of Energy Office of Inertial Fusion under agreement No. DE-FC08-85DP40200 and by the Laser Fusion Feasibility Project at the Laboratory for Laser Energetics, which has the following sponsors: Empire State Electric Energy Research Corporation, New York State Energy Research and Development Authority, Ontario Hydro, and the University of Rochester. Such support does not imply endorsement of the content by any of the above parties.

REFERENCES

1. R. S. Craxton, R. L. McCrory, and J. M. Soures, *Sci. Am.* **255**, 68–79 (1986).
2. R. L. McCrory, J. M. Soures, C. P. Verdon, P. Audebert, D. Bradley, J. Delettrez, R. Hutchison, S. D. Jacobs,

P. Jaanimagi, R. Keck, H. Kim, J. Knauer, R. Kremens, S. Letzring, F. Marshall, P. McKenty, M. C. Richardson, A. Simon, R. Short, S. Skupsky, and B. Yaakobi, *High-Intensity Laser-Matter Interactions* (SPIE, Bellingham, WA, 1988), Vol. 913; Laboratory for Laser Energetics Annual Report-1987, DOE/DP 40200-64, 93 (1988).

3. J. Nuckolls, L. Wood, A. Thiessen, and G. Zimmerman, *Nature* **239**, 139 (1972).
4. R. F. Kidder, *Nucl. Fusion* **16**, 3 (1976).
5. Laser Program Annual Report-1984, Lawrence Livermore National Laboratory, Livermore, CA, UCRL-50021-84, 5-35 (1985)
6. S. D. Jacobs, K. A. Cerqua, T. J. Kessler, W. Seka, and R. Bahr, in 16th Annual Symposium on Optical Materials for High Power Lasers, *Nat. Bur. Stand. (U.S.), Spec. Publ.* **727** (GPO, Washington, DC, 1986), p. 15.
7. LLE Review **33**, 1 (1987).
8. LLE Review **31**, 106 (1987).
9. LLE Review **33**, 11 (1987).
10. D. L. Musinski, T. M. Henderson, R. J. Simms, and T. R. Pattinson, *J. Appl. Phys.* **51**, 1394 (1980).
11. B. I. Bennett, J. D. Johnson, G. I. Kirley, and G. T. Rand, Los Alamos National Laboratory Report No. LA-7130, 1978.
12. W. F. Huebner, A. L. Merts, N. H. Magee, Jr., and M. F. Argo, Los Alamos National Laboratory Report No. LA-6760-M, 1977.
13. LLE Review **31**, 101 (1987).
14. J. D. Kilkenny, P. Bell, R. Hanjks, G. Power, R. Turner, J. Weidwald, and D. K. Bradley, *Rev. Sci. Instrum.* (to be published).
15. G. Pien, M. C. Richardson, P. D. Goldstone, R. H. Day, F. Ameduri, and G. Eden, *Nucl. Instrum. Methods* **B18**, 101 (1986).
16. M. C. Richardson, G. G. Gregory, R. L. Keck, S. A. Letzring, R. S. Marjoribanks, F. J. Marshall, G. Pien, J. S. Wark, B. Yaakobi, P. D. Goldstone, A. Hauer, G. S. Stradling, F. Ameduri, B. L. Henke, and P. A. Jaanimagi, in *Laser Interaction and Related Plasma Phenomena, Vol. 7*, edited by H. Hora and G. H. Miley (Plenum Press, New York, 1986), p. 179.
17. M. C. Richardson, R. F. Keck, S. A. Letzring, R. L. McCrory, P. W. McKenty, D. M. Roback, J. M. Soures, and C. P. Verdon, *Rev. Sci. Instrum.* **57**, 1737 (1986).
18. LLE Review **28**, 155 (1986).
19. LLE Review **31**, 93 (1987).
20. LLE Review **25**, 7 (1985).